


Conditions for dual-pumped optical parametric oscillation in Kerr microresonators

Menglong He^{*} and Kambiz Jamshidi[†]

Integrated Photonic Devices Laboratory, Technische Universität Dresden, Helmholtzstrasse 16, Dresden 01069, Germany

 (Received 14 October 2022; revised 6 September 2023; accepted 24 October 2023; published 16 November 2023)

We theoretically and numerically study the dual-pumped optical parametric oscillation in Kerr nonlinear microresonators with and without the thermo-optic effect. Parametric gain at degeneracy points, which exceeds the intrinsic loss of the waveguide, can be achieved with both normal and anomalous dispersion by optimizing the pump power, detuning, and frequency offset. Our theoretical modeling includes the various forms of dynamic behavior of the dual-pumped cavity, such as build-up, bistability, and chaotic behavior. Besides, the conditions for spectral phase transition, including the power threshold and critical point, have also been numerically investigated to achieve degenerate parametric oscillation. Notably, we analyze the phase-sensitive amplification regimes leading to phase bifurcation, which enable various applications in quantum random number generation, all-optical coherent Ising machines, and on-chip photon-pair generation. Our study will hopefully provide guidelines for Kerr-based microresonator designs, which aim for degenerate optical parametric oscillation.

DOI: [10.1103/PhysRevApplied.20.054036](https://doi.org/10.1103/PhysRevApplied.20.054036)

I. INTRODUCTION

Optical parametric oscillators (OPOs) are critical for a myriad of applications, such as optical-frequency-comb (OFC) generators [1,2], coherent Ising machines (CIMs) [3,4], random number generators [5], photonic spiking neurons [6], and frequency converters [7]. As tunable convenient sources of coherent light, OPOs have been demonstrated in a variety of platforms, ranging from electro-optic (χ^2) media such as lithium niobate (LiNbO_3) [8], aluminum nitride (AlN) [9], and aluminum gallium arsenide (AlGaAs) [10] to the Kerr (χ^3) media, including silica [11], silicon carbide (SiC) [12], silicon (Si) [13], and silicon nitride (Si_3N_4) [14]. Among the various photonic platforms, Si_3N_4 has emerged as a Kerr-based platform [15]. It enables CMOS-compatible photonic integration, ultralow propagation loss below 0.4 dBm^{-1} [16], a broad wavelength transparency range from $0.4 \mu\text{m}$ to $2.35 \mu\text{m}$ [17], watt-range power handling, and strong Kerr nonlinearity with the absence of two-photon absorption (TPA) due to its insulator nature [18,19].

Recently, there has been considerable interest in exploiting microresonator-based OPOs to realize photonic integrated circuits (PICs) that utilize stimulated [20–22] and spontaneous [23,24] four-wave mixing (FWM). To date,

single-pumped OPOs by using silicon nitride photonics have already been well studied and the conditions for parametric oscillation have been investigated [25,26]. Moreover, dual-pumped OPO using Kerr nonlinearity is a crucial case in which photons from both the blue and red pumps are converted into coherent photon pairs by FWM (Fig. 1). Specifically, degenerate OPOs (DOPOs) occur when the signal and idler photons share the same frequency [27]. Apart from the DOPOs using χ^2 nonlinearity in the first proof-of-principle demonstration [28], Kerr-based DOPOs require double pumps with different wavelengths. Silicon nitride microresonator-based DOPOs have been theoretically and experimentally demonstrated in the normal group-velocity-dispersion (GVD) regime, which can be achieved by the dispersion engineering of the silicon nitride waveguide [29]. Meanwhile, the design of Kerr-based dual-pumped DOPOs still requires further studies on the bifurcation of dual pumps, spectral phase transition, and phase-sensitive amplification.

We investigate the design considerations of dual-pumped OPOs in silicon nitride cavities by exploiting the stimulated parametric FWM. The thermo-optic effect (TOE) due to absorption loss should be considered in the design of OPOs, especially those employing intense pump powers with lossy waveguides or requiring high modeling precision. The nonlinear dynamics in Kerr microresonators due to large optical nonlinearities have been studied. These dynamics include bifurcation such as bistability [24,30], instability, dual-pumped parametric oscillation, spectral

^{*}menglong.he@tu-dresden.de

[†]kambiz.jamshidi@tu-dresden.de

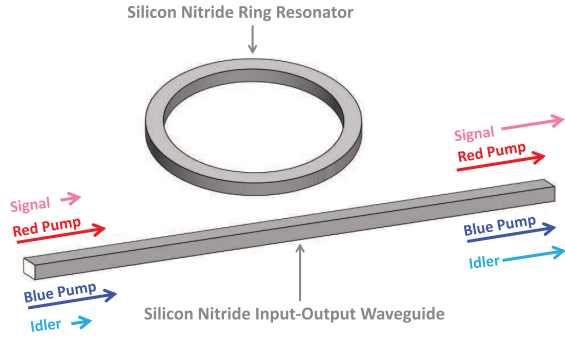


FIG. 1. An introduction to the microresonator-based dual-pumped optical parametric oscillator: the coherent input fields consist of dual pumps and signal or idler fields, which can be seeded from vacuum.

phase transitions between degenerate and nondegenerate regimes [31], and nonequilibrium phase transition [29]. Controllable spectral phase transition through the selection of the frequency offset has been studied in previous works [29,31]. In particular, we also explore the intensity-dependent critical point for tuning the phase transition as a feasible alternative. This paper is organized as follows. In Sec. II, we theoretically study the dynamics of OPOs with dual-pumped fields by a set of coupled-mode equations derived from the normalized Lugiato-Lefever equation [24,32], including TOE terms. Section III utilizes numerical simulations to analyze the complex dynamics of Kerr microresonators with two pumps and the parameter space for optical parametric gain with or without thermal stabilization. Finally, in Sec. IV, we derive the power threshold required by the parametric gain and also explore the conditions for the second-order critical points to achieve frequency-degenerate oscillation. Notably, the phase-sensitive gain of DOPOs has been modeled and simulated with both normal and anomalous GVD.

II. MATHEMATICAL MODEL

In OPOs with two continuous-wave (cw) pumps, the relation between the pumps (with angular frequency ω_r and ω_b) and the created photon pairs (with angular frequency ω_s and ω_i) is $\omega_r + \omega_b \rightarrow \omega_s + \omega_i$. As shown in Fig. 2, we focus on the mode spectra, which consists of a red pump \bar{a}_r (normalized) with detuning $\bar{\Delta}_r$ (normalized) and a blue pump \bar{a}_b with detuning $\bar{\Delta}_b$. Besides, the generated signal-idler pairs, denoted by \bar{a}_s and \bar{a}_i , have cold detunings ($\bar{\Delta}_s$ and $\bar{\Delta}_i$). The two pumps (\bar{a}_r and \bar{a}_b), the signal \bar{a}_s , and the idler \bar{a}_i have frequency offsets with the degeneracy point (ω_c) equal to \bar{k}_r , \bar{k}_b , \bar{k}_s , and \bar{k}_i , respectively, as follows:

$$\frac{\partial \bar{a}}{\partial \bar{\tau}} = \frac{\partial \bar{a}_r}{\partial \bar{\tau}} e^{i\bar{k}_r \bar{t}} + \frac{\partial \bar{a}_b}{\partial \bar{\tau}} e^{i\bar{k}_b \bar{t}} + \frac{\partial \bar{a}_s}{\partial \bar{\tau}} e^{i\bar{k}_s \bar{t}} + \frac{\partial \bar{a}_i}{\partial \bar{\tau}} e^{i\bar{k}_i \bar{t}}. \quad (1)$$

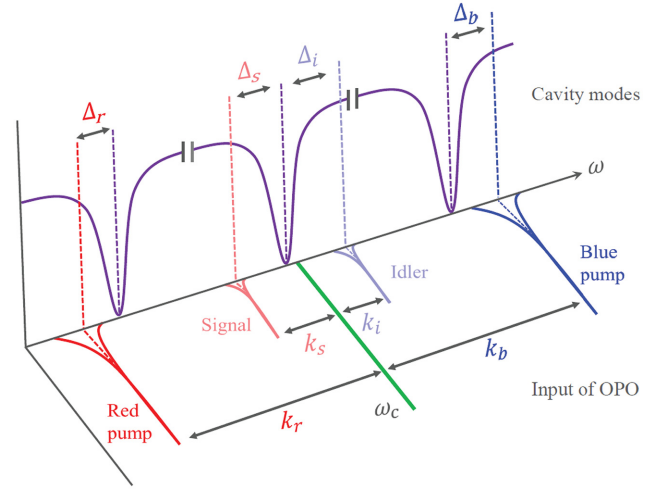


FIG. 2. Depictions of the mode spectra and frequency in a four-mode approximation. The purple curves indicate the linear transmission of ring cavities over three free spectrum ranges (FSRs). The green line highlights the degeneracy point of the DOPOs.

The degenerate OPOs occur when the frequency offsets of the signal and idler both equal 0. We exploit a set of nonlinear coupled equations [Eqs. (2)–(5)] to model the field propagation of the red pump (long-wavelength pump), the blue pump (short-wavelength pump), the signal field, and the idler field. Compared with the previous work proposed in Refs. [24,29], our model considers several additional optical effects in the Si_3N_4 ring cavities, such as propagation loss, nonzero frequency detuning, and, importantly, thermal nonlinearity, which can significantly induce a nonlinear shift of the refractive index:

$$\begin{aligned} \frac{\partial \bar{a}_r}{\partial \bar{\tau}} = & i(|\bar{a}_r|^2 + 2|\bar{a}_b|^2 + 2|\bar{a}_s|^2 + 2|\bar{a}_i|^2 + \eta \bar{k}_r^2) \bar{a}_r \\ & + i\bar{a}_s \bar{a}_i \bar{a}_b^* + (-1 - i\bar{\Delta}_r + i\bar{T}) \bar{a}_r + \bar{S}_r, \end{aligned} \quad (2)$$

$$\begin{aligned} \frac{\partial \bar{a}_b}{\partial \bar{\tau}} = & i(|\bar{a}_b|^2 + 2|\bar{a}_r|^2 + 2|\bar{a}_s|^2 + 2|\bar{a}_i|^2 + \eta \bar{k}_b^2) \bar{a}_b \\ & + i\bar{a}_s \bar{a}_i \bar{a}_r^* + (-1 - i\bar{\Delta}_b + i\bar{T}) \bar{a}_b + \bar{S}_b, \end{aligned} \quad (3)$$

$$\begin{aligned} \frac{\partial \bar{a}_s}{\partial \bar{\tau}} = & i(|\bar{a}_s|^2 + 2|\bar{a}_r|^2 + 2|\bar{a}_b|^2 + 2|\bar{a}_i|^2 + \eta \bar{k}_s^2) \bar{a}_s \\ & + i\bar{a}_r \bar{a}_b \bar{a}_i^* + (-1 - i\bar{\Delta}_s + i\bar{T}) \bar{a}_s + \bar{S}_s, \end{aligned} \quad (4)$$

$$\begin{aligned} \frac{\partial \bar{a}_i}{\partial \bar{\tau}} = & i(|\bar{a}_i|^2 + 2|\bar{a}_r|^2 + 2|\bar{a}_b|^2 + 2|\bar{a}_s|^2 + \eta \bar{k}_i^2) \bar{a}_i \\ & + i\bar{a}_r \bar{a}_b \bar{a}_s^* + (-1 - i\bar{\Delta}_i + i\bar{T}) \bar{a}_i + \bar{S}_i, \end{aligned} \quad (5)$$

where the total circulating field \bar{a} is formulated with respect to the degeneracy point. \bar{S} is the normalized input pump field and $\bar{\tau}$ represents the scaled slow-time, which describes the envelope evolution over the successive

round trip (t_R). In addition, the normalized cold detuning is defined by $\bar{\Delta}_0 = 2\tau_{ph}(\omega_{cav} - \omega_0)$. Importantly, all the variables in Eqs. (2)–(5) have been normalized to dimensionless terms (for details, see Appendix). The total cavity loss modeled by the normalized term -1 includes the coupling θ and the intrinsic loss α . In particular, the cubic terms can describe the Kerr effect, which accounts for cross-phase modulation (XPM), self-phase modulation (SPM), and optical parametric processes such as FWM. Besides, the quadratic terms of the frequency model the dispersion, a positive sign of which ($\eta = +1$) means normal GVD while a negative sign ($\eta = -1$) means anomalous GVD. Here, \bar{T} refers to the temperature in silicon nitride cavities heated by the surface photon absorption, leading to a red shift of the cavity resonance [33]. We can describe the thermal evolution by using Newton's law of cooling, as [34,35]:

$$\frac{\partial \bar{T}}{\partial \bar{\tau}} = (\bar{\chi}_s |\bar{a}|^2 - \bar{T}) \frac{1}{\bar{\tau}_{th}}. \quad (6)$$

In particular, the ratio of detuning caused by the TOE induced by self-heating and that of the Kerr effect can be quantified by the thermal coefficient $\bar{\chi}_s$ [33,34]:

$$\bar{\chi}_s = \frac{k_a \alpha \tau_{th} dn/dT}{c_v \rho n_2}. \quad (7)$$

Here, dn/dT is the thermorefractive coefficient, n_2 represents the Kerr-nonlinearity coefficient [36,37], k_a gives the absorption fraction of silicon nitride [33], and τ_{th} is the thermal relaxation time. The specific heat is referred to as $c_v \rho$. In the equilibrium states, the TOE (delayed response) and the Kerr effect (instantaneous response) are both proportional to the cubic term of the total field, $|\bar{a}|^2 a$. With the thermal coefficient $\bar{\chi}_s$ less than 1, the Kerr effect is the most

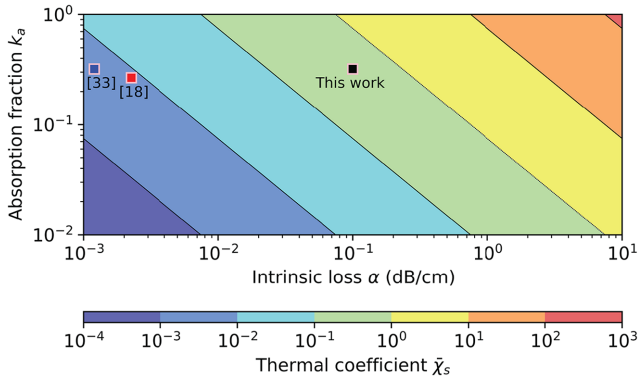


FIG. 3. The thermal coefficient $\bar{\chi}_s$ of silicon nitride ring resonators, as a function of the intrinsic loss of the waveguide α and the absorption ratio k_a . The red and blue points indicate the intrinsic loss, absorption loss, and corresponding thermal coefficient considered in the state-of-the-art works [18,33].

TABLE I. The key parameters and constants used in the simulation.

Parameter	Symbol	Value
Resonance frequency	ω_0	$2\pi \times 193.55$ THz
Ring radius	R	100 μm
Mode effective area	A_{eff}	1.15×10^{-12} m ²
Group-velocity dispersion	$ \beta_2 $	0.55 ps ² /m
Intrinsic loss	α	0.1 dB/cm
Absorption fraction	k_a	0.32
Ring-bus power coupling	θ	0.00144
Photon lifetime	τ_{ph}	1.52 ns
Specific heat	$c_v \rho$	1.84×10^{15} W/m ³ [35]
Thermal relaxation time	τ_{th}	1.354 μs [36]
Group index	n_g	2.1
Kerr-nonlinearity coefficient	n_2	2.4×10^{-19} m ² /W [36]
Thermorefractive coefficient	dn/dT	2.5×10^{-5} K ⁻¹ [35]

dominant optical nonlinearity in silicon nitride waveguides within the whole intensity range. Figure 3 depicts the thermal coefficient $\bar{\chi}_s$ of silicon nitride waveguides in terms of the intrinsic loss α and the absorption fraction k_a . The intrinsic loss consists of absorption loss induced by surface photon absorption due to hydrogen impurities in silicon nitride and scattering loss caused by the side-wall roughness of the waveguide [18]. The important variables and constants utilized in the numerical simulation are summarized in Table I. For a silicon nitride ring cavity with a radius of 100 μm , an intrinsic loss α of 0.1 dB/cm, an absorption fraction k_a of 0.32, and a coupling coefficient θ equal to 0.00144 for critical coupling, the ratio between the strength of the TOE and the Kerr effect is 0.4286. This indicates that the Kerr nonlinearity is more significant than the TOE in silicon nitride ring cavities with a high quality factor, which agrees with the measurement results shown in the previous works with ultralow loss [18,33].

III. DYNAMICS AND PARAMETRIC GAIN

We now study the conditions for the maximum optical parametric gain. It is worth noting that the parametric oscillation occurs when the gain exceeds the intrinsic loss of the cavity. Otherwise, the signal field reduces to a squeezed vacuum-state field due to spontaneous FWM [38,39]. By exploiting the perturbation theory, we investigate the nonlinear dynamics of dual pumps, such as resonance, bistability, and oscillation in the Kerr microresonators due to XPM, SPM, and the TOE. Our primary goal is to investigate the regions for parametric gain in the parameter space (without normalization) defined by the pump power P_{in} , the frequency detuning Δ , the angular frequency offset k , and the relative phase ϕ .

A. Dynamics of ring cavities with dual pumps

We assume that both pumps are undepleted by the χ^3 -based parametric interaction, which is an efficient approximation for typical experiments not requiring a high conversion efficiency [31,40]. We perform the perturbation analysis [41] to analyze the complex dynamics of the Kerr cavities with coupled modes. We can derive the dimensionless steady-state field equation of the red and blue pumps using perturbation theory (with the signal or idler typically in the submicrowatt range):

$$\begin{bmatrix} \bar{I}_r^2 + 2\bar{\delta}_r\bar{I}_r + \bar{\delta}_r^2 + 1 & 4\bar{I}_b\bar{I}_r + 4\bar{I}_r^3 + 4\bar{\delta}_r\bar{I}_r \\ 4\bar{I}_b\bar{I}_r + 4\bar{I}_r^3 + 4\bar{\delta}_r\bar{I}_r & \bar{I}_b^2 + 2\bar{\delta}_b\bar{I}_b + \bar{\delta}_b^2 + 1 \end{bmatrix} \begin{bmatrix} \bar{I}_r \\ \bar{I}_b \end{bmatrix} = \begin{bmatrix} |\bar{S}_r|^2 \\ |\bar{S}_b|^2 \end{bmatrix}, \quad (8)$$

where \bar{I}_r is the intensity of the red pump and \bar{I}_b is the intensity of the blue pump. For concreteness, the extra terms $\bar{\delta}_r$ and $\bar{\delta}_b$ are defined by $\eta\bar{k}_r^2 - \bar{\Delta}_r$ and $\eta\bar{k}_b^2 - \bar{\Delta}_b$, respectively. By solving the coupled quartic equations, which govern the various forms of bifurcation behavior of the system, we can obtain the optical resonance curves of both the red and the blue pumps. The numerical simulation of the parametric gain focuses on a microring cavity formed by a 100- μm -radius ring of silicon nitride waveguide with a 700×690 nm cross section. Besides, the coupling coefficient θ is considered to be 0.00144 and the propagation loss α is 0.1 dB/cm. The group-velocity dispersion $|\beta_2|$ is 0.55 ps²/m. We also assume, for convenience, that the input powers of the red and blue pumps are identical. The red and blue pumps are offset from the central frequency point by one FSR (defined as F).

As illustrated in Fig. 4, we study two critical conditions of pump detuning with and without thermal stabilization: (1) with the red and blue pumps sharing the same detuning ($\Delta_r = \Delta_b$), which has been considered in Ref. [29]; and (2) with the red and blue pumps sharing the opposite detuning ($\Delta_r = -\Delta_b$). The stable-equilibrium states of the red and blue pump power in intracavity have been visualized with three different input powers: 0.65, 1.3, and 2.6 mW (from light to dark colors). Notably, the purple lines illustrate the bistable jumps of the intracavity power arising from the Kerr-induced bistability. In contrast, the ring cavity does not exhibit optical bistability under the same pump conditions with thermal stabilization. Moreover, according to Fig. 4, we can conclude that the detuning condition ($\Delta_r = -\Delta_b$) cannot be utilized for the generation of dual-pumped parametric oscillation (with a low total circulating power). As the input pump power P_{in} increases, the intensity-dependent resonance shifting becomes visible and the bistable curves bend to the right because of the thermal effect. To effectively generate parametric oscillation, the circulating power of both

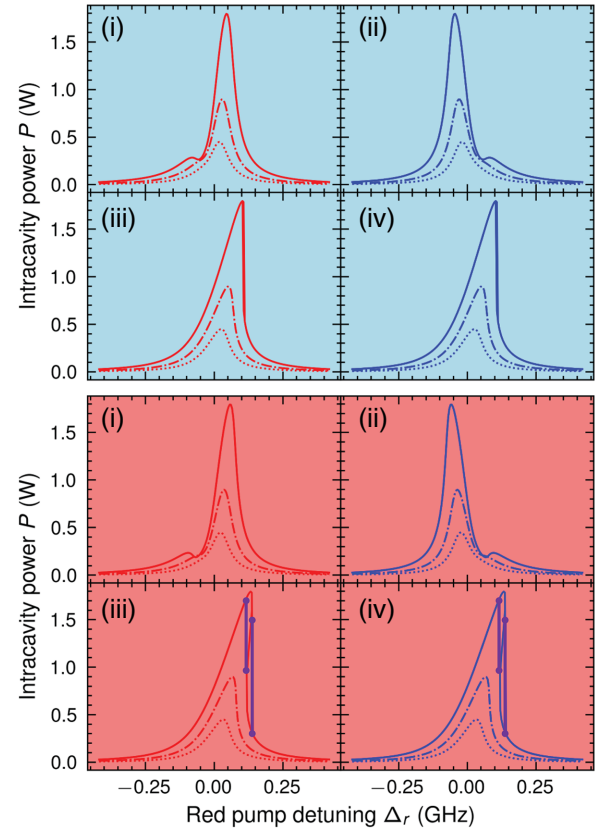


FIG. 4. The intracavity power for the red and blue pumps (input power for both red and blue pumps are equal to 0.65, 1.3, and 2.6 mW), respectively, without and with the thermo-optic effect (TOE). The upper figures with a blue background describe the simulation results with thermal stabilization. The lower figures with a red background show the results with the TOE: (i) red pump with cold detuning $\Delta_r = -\Delta_b$; (ii) blue pump with $\Delta_r = -\Delta_b$; (iii) red pump with $\Delta_r = \Delta_b$; (iv) blue pump with $\Delta_r = \Delta_b$. The purple dashed lines highlight bistable jumps.

the red and blue pumps should be maximized above the threshold.

In Fig. 5, we present the simulation results of the nonlinear dynamics without and with the TOE using bifurcation analysis, widely applied in the modeling of optical cavities [42,43]. Figure 5 introduces the dynamics map in silicon nitride ring cavities with dual pumps, including bistability in red (BS), stability in blue (SB), and instability in purple (IB). Remarkably, we observe a larger region of both BS and IB arising under the preferred detuning condition $\Delta_r = \Delta_b$. As the pump power increases, the regimes of BS and IB expand. Notably, the chaotic regions of the dual pumps (in purple) can be efficiently compressed by exploiting the thermal stabilization.

B. Parametric gain and phase matching

In this subsection, we will study the parametric gain under both normal and anomalous GVD conditions. Linear

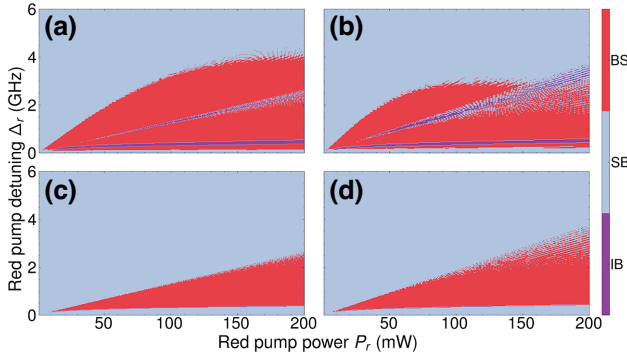


FIG. 5. The dynamics map of bistability (BS), stability (SB), and instability (IB) in the Si_3N_4 ring cavities with dual pumps (same power): (a) first scenario with $\Delta_r = \Delta_b$, with thermal stabilization; (b) first scenario with $\Delta_r = \Delta_b$, without thermal stabilization; (c) second scenario with $\Delta_r = -\Delta_b$, with thermal stabilization; (d) second scenario with $\Delta_r = -\Delta_b$, without thermal stabilization.

stability analysis is utilized to derive the gain coefficient g , which can be derived by [31,44]:

$$\partial \begin{bmatrix} \bar{a}_s \\ \bar{a}_i^* \end{bmatrix} = \begin{bmatrix} -1 - i\bar{\Gamma}_s & \bar{a}_r \bar{a}_b \\ \bar{a}_r^* \bar{a}_b^* & -1 + i\bar{\Gamma}_i \end{bmatrix} \begin{bmatrix} \bar{a}_s \\ \bar{a}_i^* \end{bmatrix} \partial \tau + \begin{bmatrix} \bar{S}_s \\ \bar{S}_i^* \end{bmatrix} \partial \tau, \quad (9)$$

$$g = -1 + \sqrt{|\bar{a}_r|^2 |\bar{a}_b|^2 - (\bar{\Gamma})^2}, \quad (10)$$

where $\bar{\Gamma}_s$, defined as the phase-mismatch term of the signal, can be calculated via $\bar{\Delta}_s - \eta \bar{k}_s^2 - 2|\bar{a}_r|^2 - 2|\bar{a}_b|^2 - \bar{T}$. Similarly, the phase-mismatch term $\bar{\Gamma}_i$ of the idler is given by $\bar{\Delta}_i - \eta \bar{k}_i^2 - 2|\bar{a}_r|^2 - 2|\bar{a}_b|^2 - \bar{T}$. In addition, the parameter $\bar{\Gamma}$ denotes the average phase mismatch: $\bar{\Gamma} = (\bar{\Gamma}_s + \bar{\Gamma}_i)/2$. By analyzing the eigenvalues of the Jacobian matrix [see Eq. (9)], we derive the solutions of the signal and idler fields, which take an exponential form [31]. Furthermore, the parametric gain coefficient g represents the net gain of the signal-idler pairs per round-trip time [25].

The phase-matching condition should be fulfilled to maximize the gain coefficient g for varying pump power and detuning. The numerical simulation of optimal gain versus pump power P_r and detuning Δ_r is illustrated in Fig. 6 for the maximization of the conversion efficiency from the pumps to the signal. Besides, the dispersion of the waveguide can be engineered [45]. Figure 6 shows the optimal parametric gain g_{\max} , with anomalous GVD existing in a more extensive parameter space. In contrast, the parametric amplification with normal dispersion is limited at low detuning, below the instability region (in purple dots). Significantly, the parametric amplification regions and the maximum parametric gain have been efficiently enlarged by exploiting thermal stabilization.

We thoroughly investigate three prerequisites for the maximum parametric gain of dual-pumped OPOs: critical

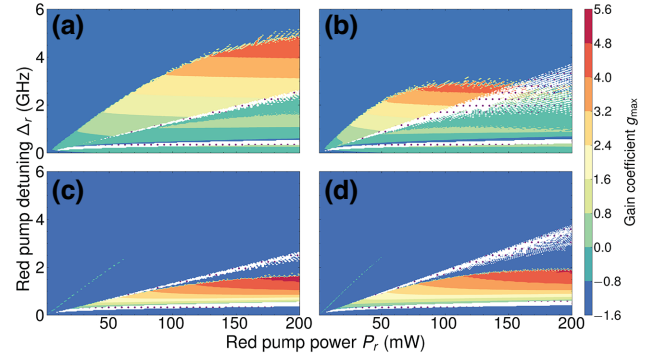


FIG. 6. The optimal parametric gain g_{\max} of the silicon nitride resonator with $\Delta_r = \Delta_b$ (the blank space with dots represents the instability region): (a) g_{\max} (anomalous dispersion) with thermal stabilization; (b) g_{\max} (anomalous dispersion) without thermal stabilization; (c) g_{\max} (normal dispersion) with thermal stabilization; (d) g_{\max} (normal dispersion) without thermal stabilization.

coupling, on resonance, and the phase-matching condition. The silicon nitride microresonator operates near the critical coupling. The optimal gain coefficient is analyzed in the parameter space defined by red pump detuning Δ_r and blue pump detuning Δ_b . As mentioned in the previous section, the maximum build-up of dual pumps does not exist with the negative detuning condition: $\Delta_r = -\Delta_b$. Therefore, we simulate the gain coefficient g by sweeping the red and blue pump detuning from 0 to 3 GHz and the red and blue pump power is fixed at 25 mW and 50 mW, respectively. Figure 7 depicts the preferred pump-detuning condition for the maximum parametric gain g : the red and blue pumps have the same positive detuning ($\Delta_r = \Delta_b$) with intense pump power. Furthermore, we can see that the instability region (illustrated by the dotted space) expands with thermal nonlinearity or by increasing the pump power. Notably, in the anomalous-dispersion region, the parametric gain coefficient g is 5 times larger than that with normal dispersion. Interestingly, the inclusion of the TOE enlarges the parameter space of the pump detuning for parametric gain while causing more severe instability.

IV. POWER THRESHOLD AND PHASE TRANSITION

As a first step toward the spectral phase-transition analysis, we investigate the minimum power threshold P_{th} , taking into account the phase-matching condition ($\bar{\Gamma} = 0$) of the dual-pumped OPO without and with thermal stabilization. We construct the universal gain map for various pump powers and detuning values in Fig. 8 to fully characterize the optimal parametric gain g_{\max} , the power threshold (indicated by a pink dashed line), and the phase mismatch $\bar{\Gamma}$ (indicated by a white dashed line). Notably, we summarize the defining features of the gain

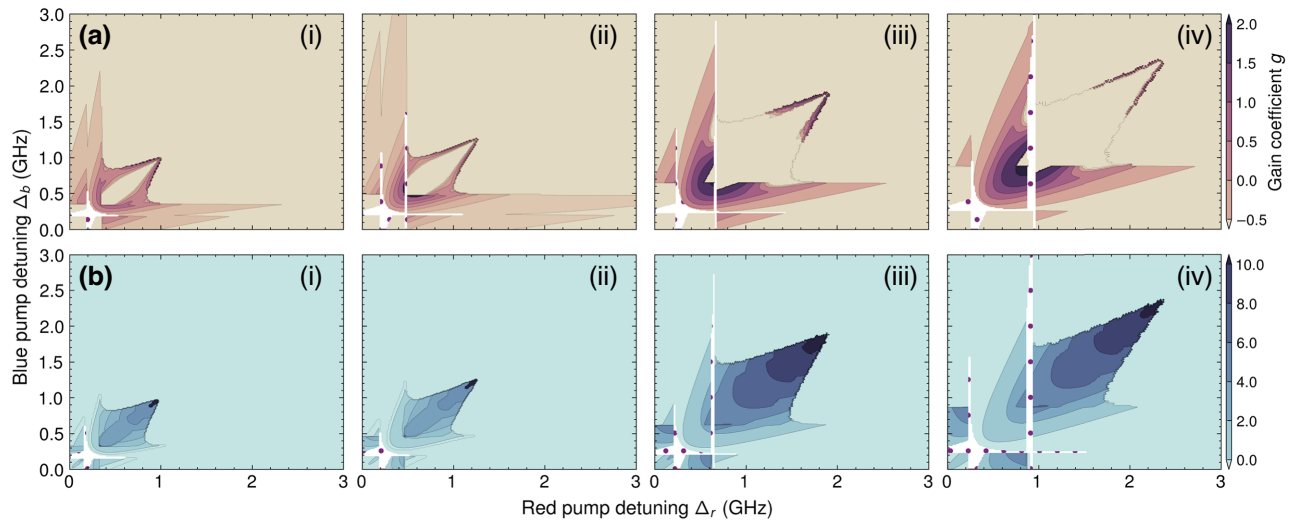


FIG. 7. (a) The optical parametric gain g as a function of the red and blue pump detuning (Δ_r and Δ_b) with various pump powers P_r in the normal-dispersion region: (i) $P_{in} = 25$ mW without TOE; (ii) $P_{in} = 25$ mW with TOE; (iii) $P_{in} = 50$ mW without TOE; (iv) $P_{in} = 50$ mW with TOE. (b) The optical parametric gain g as a function of the red and blue pump detuning (Δ_r and Δ_b) with various pump powers in the anomalous dispersion: (i)–(iv) are defined as in (a). The blank space with dots indicates the instability region.

map near critical coupling. First, the dual-pumped parametric oscillation of the Kerr-based microresonator with normal dispersion requires positive detuning. In comparison, the optical parametric gain, which exceeds the intrinsic waveguide loss, exists in both positive and negative detuning in anomalous regimes. Next, the power threshold P_{th} rises dramatically with an increasing propagation loss α

from 0.1 to 0.3 dB/cm. Third, to achieve the optimal parametric gain g_{max} , the warm-detuning term $\bar{\Delta}_{warm}$, defined as $\bar{\Delta}_s - \bar{T} - 2|\bar{a}_r|^2 - 2|\bar{a}_b|^2$, should have the same sign as the GVD of the waveguide. In contrast to the parametric gain maps considering the TOE, the gain profiles with thermal stabilization indicate that the exclusion of the TOE can enable a broader region for parametric gain (with normal

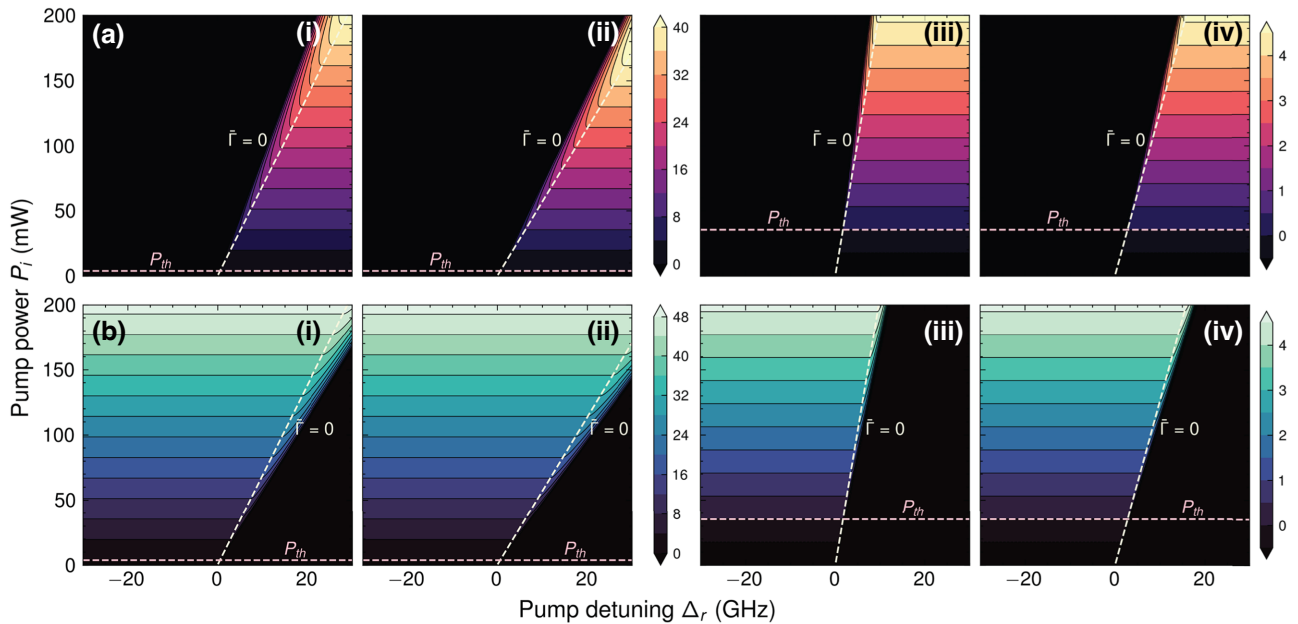


FIG. 8. The optimal parametric gain map (power threshold P_{th} and phase-matching conditions) as a function of the minimal pump power P_i and pump detuning Δ_r in the (a) anomalous-dispersion $\beta < 0$ and (b) normal-dispersion $\beta > 0$ regions. In both (a) and (b): (i) $\alpha = 0.1$ dB/cm without TOE; (ii) $\alpha = 0.1$ dB/cm with TOE; (iii) $\alpha = 0.3$ dB/cm without TOE; (iv) $\alpha = 0.3$ dB/cm with TOE. The dashed pink lines indicate the power threshold and the dashed white lines highlight the phase-matching regions.

dispersion) on the red side of resonance. Thermal nonlinearity, however, introduces a more extensive parametric gain regime with anomalous dispersion.

According to Eqs. (9) and (10), we can derive the power threshold and the critical point (at which phase bifurcation occurs) under the on-resonance condition of ring cavities with critical coupling:

$$\begin{aligned} P_{\text{th}} &= A_{\text{eff}}^2 t_R^2 / 8 \gamma v_g \tau_{\text{ph}}^3 \theta, \\ P_{\text{cr}} &= A_{\text{eff}} \Delta_r t_R^2 / (16 + 8 \bar{\chi}_s) \gamma v_g \tau_{\text{ph}}^2 \theta, \end{aligned} \quad (11)$$

where A_{eff} is the effective area, $1.15 \times 10^{-8} \text{ cm}^2$, and γ is the nonlinear refraction, equal to $2.4 \times 10^{-15} \text{ cm/W}$. In addition, feedback circuits, such as the proportional-integral-derivative (PID) controller [24], can stabilize and tune the cavity resonance to ensure the maximum build-up in the microresonator. As shown in Fig. 9, the simulated power threshold of the parametric oscillation in the Kerr microresonator is significantly sensitive to intrinsic loss of the silicon nitride waveguide, while the second-order critical point power P_{cr} with, e.g., pump detuning Δ_r equal 4 GHz, increases with a lower slope compared with the power threshold. Furthermore, phase-sensitive parametric amplification and the spectral phase transition exist when the warm detuning $\bar{\Delta}_{\text{warm}}$ and waveguide dispersion β_2 have the opposite sign above the power threshold. Additionally, both the threshold and critical point increase with a larger cavity length.

A. Spectral phase transition

In this section, we investigate the spectral phase transition in the Kerr-based DOPOs around the second-order

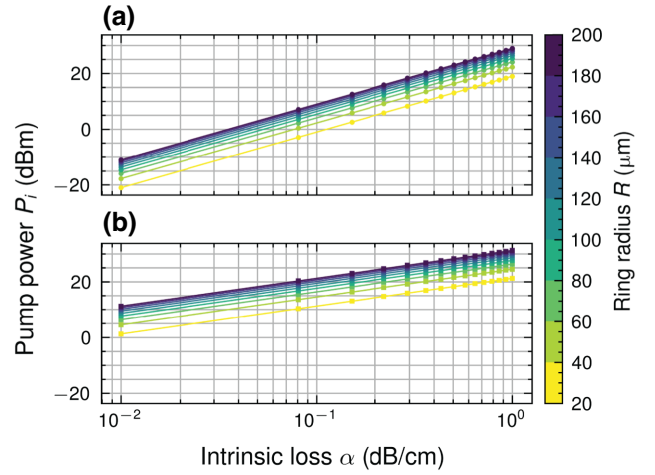


FIG. 9. (a) The power threshold P_{th} of the parametric oscillation and (b) the critical-point power P_{cr} versus the waveguide loss α , with thermal stabilization, in ring cavities with radius R ranging from 20 to 200 μm .

critical point. This analysis can demarcate a clear boundary between the degenerate and nondegenerate parametric oscillation [31]. The gain spectrum with and without the TOE, as shown in Fig. 10, presents distinctive features of phase transition induced by the interplay between the waveguide dispersion β_2 , the detuning Δ_r , and the on-resonance pump power P_i . Besides, the principle of spectral phase transition can be explained by the gain spectrum: the double-peak gain with anomalous dispersion (blue figures), which fulfills the phase-matching condition, represents nondegeneracy, while the single-peak gain with normal dispersion (red figures), by contrast, corresponds

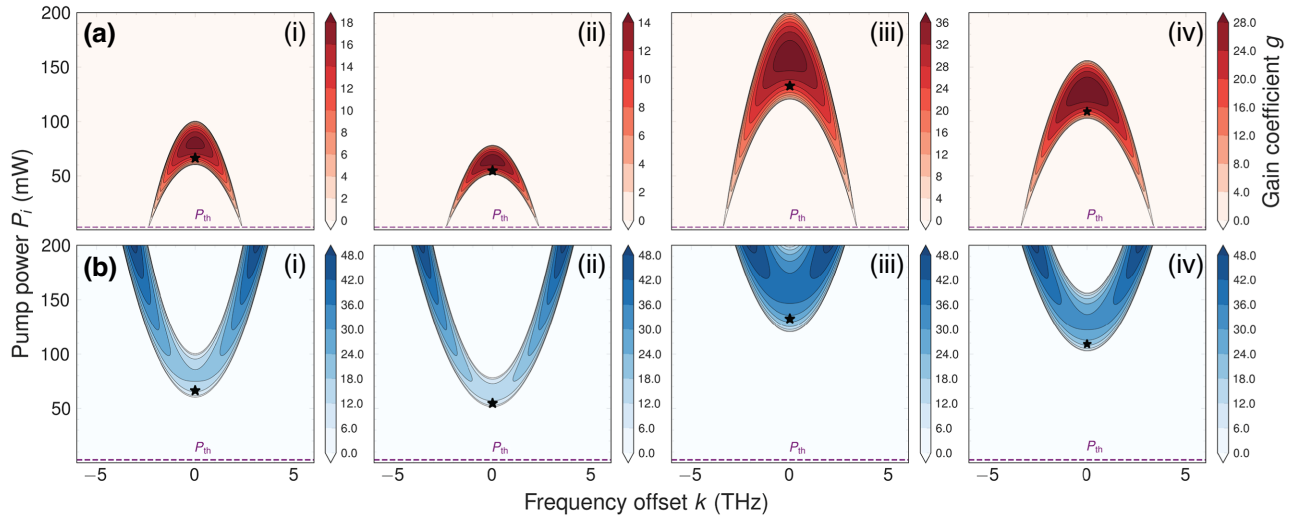


FIG. 10. The spectrum of the optical parametric gain g for varying pump power, pump detuning, and dispersion values, with and without thermal stabilization. The red plots (a) denote normal GVD and the blue plots (b) represent anomalous GVD. In both (a) and (b): (i) $\Delta_r = 4$ GHz without TOE; (ii) $\Delta_r = 4$ GHz with TOE; (iii) $\Delta_r = 8$ GHz without TOE; (iv) $\Delta_r = 8$ GHz with TOE. The black star indicates the second-order critical point of the spectral phase transition. The power threshold is denoted with dashed purple lines.

to degeneracy. The optimal gain g_{\max} of the degenerate regime can be improved by increasing the pump detuning and power due to phase mismatch. In addition, the inclusion of thermal stabilization raises the critical point for phase transition, contributing to a higher parametric gain in the normal-dispersion regime.

Figure 11 provides detailed conditions for the second-order phase transition, which involves both normal and anomalous dispersion, and thereby the design considerations for Kerr-based DOPOs. We have identified three notable features with regard to the thermal stabilization. First, we can engineer the gain spectrum of the OPOs by controlling the phase mismatch with both normal and anomalous dispersion, thereby exploiting the phase transition from nondegeneracy to degeneracy. Second, as the on-resonance pump power P_i increases, the dual-pumped OPOs operating in the anomalous-dispersion

regime ($\beta_2 < 0$) transition from the single-peak gain to a double-peak spectrum at the critical point. On the other hand, with normal dispersion ($\beta_2 > 0$), the Kerr-based OPOs are in the nondegenerate operation with low pump power and then transit to the degeneracy region. However, due to phase mismatch, the degenerate parametric gain reduces to a value lower than the intrinsic loss of the waveguide with increasing pump power.

B. Nonequilibrium phase transition

The generated signal-idler photon pairs in DOPOs are locked to the dual pumps in terms of their frequency and phase, which bifurcates into two possible states of the signal phase: $|0\rangle$ and $|\pi\rangle$ [29]. Implementing the biphasic-state transition requires the dual-pumped OPOs to operate in the degenerate-OPO regions, as highlighted in Fig. 11. Essentially, the phase-sensitive amplification in the DOPO can explain this nonequilibrium phase-bifurcation behavior. Based on the linear stability analysis proposed in Sec. III, we can derive the phase-sensitive gain G as a function of the relative phase ϕ and time τ , shown as [46]

$$G(\phi, \tau) = |\mu(\tau)|^2 + |v(\tau)|^2 + 2|\mu(\tau)||v(\tau)|\cos(\phi), \quad (12)$$

where the four elements in the matrix can be expressed as $\mu(\tau) = \cosh(g\tau) + i\bar{\Gamma}(\sinh(g\tau)/g)$ and also the other term $v(\tau) = i(\bar{a}_r\bar{a}_b/g)\sinh(g\tau)$. When the initial phase of the dual pump is zero, we will have the relative phase, defined as $\phi = 2\phi_s + \phi_\mu - (\pi/2)$. This allows us to calculate the phase-sensitive gain g of the χ^3 -based DOPO. As shown in Fig. 12, the phase-sensitive gain G (in the round trip) only exists in two signal states with a π phase spacing, which is defined as a biphasic state [29,47].

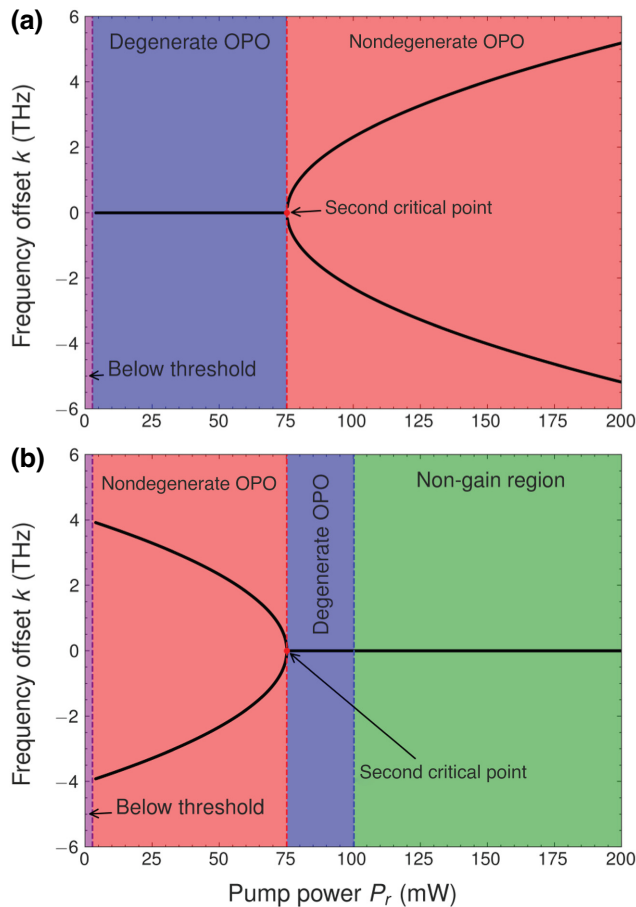


FIG. 11. An illustration of spectral phase transition between nondegeneracy and degeneracy in a dual-pumped OPO: (a) spectral transition using anomalous dispersion; (b) spectral transition using normal dispersion. DOPOs and nondegenerate OPOs can operate in the blue and red regions, respectively. The purple and green regions correspond to below-threshold and nongain regions. The second critical point has been highlighted in red.

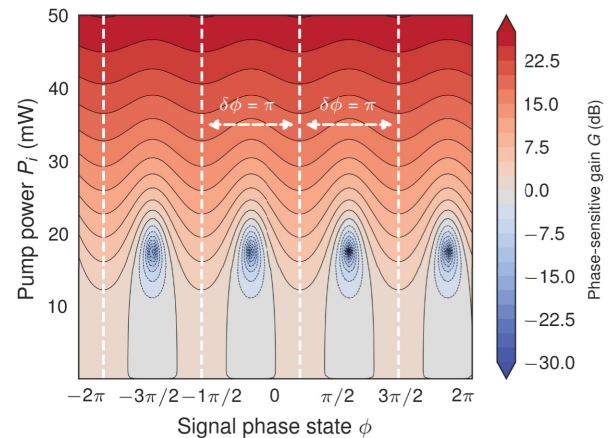


FIG. 12. The phase-sensitive amplification gain in Kerr-based ring cavities, as a function of the signal phase ϕ and pump power P_i . The white dashed lines highlight the gradient.

V. CONCLUSIONS

In conclusion, we have comparatively investigated the design considerations to achieve degenerate parametric oscillation without and with thermal stabilization in the silicon nitride microresonator. As a first step, we have investigated the complex bifurcation of dual pumps with rich nonlinear dynamics. Next, with regard to the power threshold and the second-order critical point, the conditions for the optimal parametric gain have been studied, including anomalous and normal dispersion. Besides, we conclude that the parametric gain in anomalous dispersion exists in a larger parameter space of pump powers and detuning. In particular, the DOPOs with optimum parametric gain exist in the normal-dispersion regime. Notably, we have studied the phase transition of the Kerr-based OPOs. Furthermore, the phase-sensitive amplification in the resonator-based DOPOs has been simulated.

ACKNOWLEDGMENTS

We thank Mircea-Traian Catuneanu and Ryan Hamerly for their valuable discussions. This work is supported in part by the Federal Ministry of Education and Research (BMBF) in the context of the projects ‘‘Silhouette’’ and ‘‘6G-Quiet.’’ Furthermore, it is also funded by the Deutsche Forschungsgemeinschaft (DFG, German Research Foundation) in the context of the project ‘‘Towards Scalable Ising Machines in Silicon Using CMOS-Based Photonic Integrated Circuits.’’

APPENDIX: ANALYTICAL DESCRIPTION OF FIELD PROPAGATION IN KERR MICRORESONATORS

In order to investigate the propagation of internal fields in Kerr microresonators numerically, we start with the simple Lugiato-Lefever equation (LLE) [48–50]:

$$\begin{aligned} \frac{\partial A(\tau, \Psi)}{\partial t} = & \sqrt{\frac{\kappa \eta P_{\text{in}}}{\hbar \omega_0}} - \left(\frac{\kappa}{2} + i \Delta_0 \right) A(\tau, \Psi) \\ & - i \frac{D_2}{2} \frac{\partial^2 A(\tau, \Psi)}{\partial \phi^2} + i g_{\text{Kerr}} |A(\tau, \Psi)|^2 A(\tau, \Psi), \end{aligned} \quad (\text{A1})$$

where $|A(\tau, \Psi)|^2$ is the intracavity energy, denoted by E_0 in units of the photon number and τ gives the slow-time on round-trip time scales. Ψ is a corotating angular coordinate. Besides, Table II summarizes the variables and their physical definitions in the LLE using the device parameters previously mentioned in Sec. II.

To derive the dynamics of the field numerically, we then switch to the master equation for the internal field intensity $a(\tau, t)$, defined on slow-time τ and fast-time t (within a single round-trip) [32,45]. This conversion

TABLE II. The list and descriptions of variables in Eqs. (A1).

Parameter	Symbol	Definition
Photon number	$ A(\Psi, t) ^2$	$E_0/\hbar\omega_0$
Pump detuning	Δ_0	$\omega_0 - \omega_p$
Photon escape rate	κ	$(\alpha L + \theta)/t_R$
Photon coupling rate	κ_{ex}	θ/t_R
Coupling efficiency	η	$\kappa_{\text{ex}}/\kappa$
Second-order dispersion	D_2	$-\beta_2 c (2\pi F)^2/n_0$
Kerr frequency shift per photon	g_{Kerr}	$\hbar\omega^2 cn_2/n_0^2 V_{\text{eff}}$

can be achieved by considering the relationship $E_0 = \hbar\omega_0 |A(\Psi, t)|^2 = A_{\text{eff}} t_R |a(\tau, t)|^2$ with additional degrees of freedom for the temperature T [34,36]:

$$\begin{aligned} \frac{\partial a(\tau, t)}{\partial \tau} = & \left[-\frac{\alpha L + \theta}{2t_R} + \frac{i\Theta}{t_R} \right] a - \frac{i\beta_2 v_g}{2} \frac{\partial^2 a}{\partial t^2} + i\gamma v_g |a|^2 a \\ & + i\delta_T a T + \frac{\sqrt{\theta}}{t_R} s_{\text{in}}, \\ \frac{\partial T}{\partial \tau} = & \frac{1}{c_v \rho} \left[k_a \alpha \frac{\int |a(\tau, t)|^2 dt}{t_R} \right] - \frac{1}{\tau_{\text{th}}} T. \end{aligned} \quad (\text{A2})$$

Here, Θ is the phase shift per round trip and v_g is the group velocity. $\gamma = \omega_0 n_2/c$ is the nonlinear refraction. The temperature of the cavity is denoted as T and s_{in} describes the input field intensity in the bus waveguide. Besides, the other variables, such as α , θ , δ_T , $c_v \rho$, and k_a , have been defined in Sec. II. For convenience, the above equation can be further rewritten in dimensionless form through normalization. In particular, the normalized master equations have been derived as follows:

$$\begin{aligned} \frac{\partial \bar{a}}{\partial \bar{\tau}} = & i(|\bar{a}|^2 + \eta \bar{k}^2 + \delta_T T) \bar{a} + (-1 - i\bar{\Delta}) \bar{a} + \bar{s}_{\text{in}}, \\ \frac{\partial \bar{T}}{\partial \bar{\tau}} = & \frac{1}{\bar{\tau}_{\text{th}}} (\bar{\chi}_s |\bar{a}|^2 - \bar{T}), \end{aligned} \quad (\text{A3})$$

where the slow-time τ is scaled to the photon lifetime τ_{ph} as $\bar{\tau} = \tau/\xi_\tau$. The fast-time t is normalized to the dispersion by $\bar{t} = t/\xi_t$. Moreover, k , which defines the linear phase difference accumulated over fast-time, is scaled as $\bar{k} = k\xi_t$. The intracavity field $\bar{a} = a/\xi_a$ and the input field $\bar{s}_{\text{in}} = s_{\text{in}}/\xi_{\text{in}}$ are normalized to the Kerr effect. In addition, the temperature T is scaled to reflect the strength of the thermo-optic effect by $\bar{T} = T/\xi_T$. All the variables are dimensionless and the normalization coefficients are listed in Table III. Next, we further consider the case of dual-pumped four-wave-mixing (FWM) as $\omega_r + \omega_b \rightarrow \omega_s + \omega_i$. By substituting the normalized total intracavity field of dual pumps, signal, and idler [described in Eq. (1)], the set of coupled-mode equations in Eqs. (2)–(5) can finally be derived based on the introduction of modal expansion

TABLE III. The definitions and coefficients of normalization used in Eqs. (A3).

Symbol	Meaning	Definition	Value
ξ_τ	Normalization of slow-time	$2\tau_{\text{ph}}$	2.68 ns
ξ_t	Normalization of fast-time	$\sqrt{ \beta_2 v_g\tau_{\text{ph}}}$	1.58 s
ξ_a	Normalization of circulating field	$(2\gamma v_g\tau_{\text{ph}})^{-1/2}$	$1.54 \times 10^4 \text{ W}^{1/2} \text{ cm}^{-1}$
ξ_{in}	Normalization of input-output field	$\sqrt{t_R^2/8\gamma v_g\tau_{\text{ph}}^3\bar{\theta}}$	$584 \text{ W}^{1/2} \text{ cm}^{-1}$
ξ_T	Normalization of temperature deflection	$(2\delta_T\tau_{\text{ph}})^{-1}$	23 mK

while neglecting the high-order nonlinear terms of the signal and idler using nonlinear-waveguide perturbation theory [25].

- [1] A. Rizzo, A. Novick, V. Gopal, B. Y. Kim, X. Ji, S. Daudlin, Y. Okawachi, Q. Cheng, M. Lipson, and A. L. Gaeta, *et al.*, Massively scalable Kerr comb-driven silicon photonic link, *Nat. Photonics* **17**, 781 (2023).
- [2] Ó. B. Helgason, M. Girardi, Z. Ye, F. Lei, J. Schröder, and V. Torres-Company, Surpassing the nonlinear conversion efficiency of soliton microcombs, *Nat. Photonics* **17**, 1 (2023).
- [3] A. Marandi, Z. Wang, K. Takata, R. L. Byer, and Y. Yamamoto, Network of time-multiplexed optical parametric oscillators as a coherent Ising machine, *Nat. Photonics* **8**, 937 (2014).
- [4] T. Honjo, T. Sonobe, K. Inaba, T. Inagaki, T. Ikuta, Y. Yamada, T. Kazama, K. Enbutsu, T. Umeki, and R. Kasahara, *et al.*, 100 000-spin coherent Ising machine, *Sci. Adv.* **7**, eabh0952 (2021).
- [5] N. Englebert, F. De Lucia, P. Parra-Rivas, C. M. Arabi, P.-J. Sazio, S.-P. Gorza, and F. Leo, Parametrically driven Kerr cavity solitons, *Nat. Photonics* **15**, 857 (2021).
- [6] T. Inagaki, K. Inaba, T. Leleu, T. Honjo, T. Ikuta, K. Enbutsu, T. Umeki, R. Kasahara, K. Aihara, and H. Takesue, Collective and synchronous dynamics of photonic spiking neurons, *Nat. Commun.* **12**, 1 (2021).
- [7] P. S. Halasyamani, New nonlinear opportunities in the ultraviolet, *Nat. Photonics* **17**, 639 (2023).
- [8] J. Lu, A. Al Sayem, Z. Gong, J. B. Surya, C.-L. Zou, and H. X. Tang, Ultralow-threshold thin-film lithium niobate optical parametric oscillator, *Optica* **8**, 539 (2021).
- [9] A. W. Bruch, X. Liu, J. B. Surya, C.-L. Zou, and H. X. Tang, On-chip χ (2) microring optical parametric oscillator, *Optica* **6**, 1361 (2019).
- [10] S. May, M. Kues, M. Clerici, and M. Sorel, Second-harmonic generation in algaas-on-insulator waveguides, *Opt. Lett.* **44**, 1339 (2019).
- [11] M.-G. Suh, Q.-F. Yang, K. Y. Yang, X. Yi, and K. J. Vahala, Microresonator soliton dual-comb spectroscopy, *Science* **354**, 600 (2016).
- [12] M. A. Guidry, K. Y. Yang, D. M. Lukin, A. Markosyan, J. Yang, M. M. Fejer, and J. Vučković, Optical parametric oscillation in silicon carbide nanophotonics, *Optica* **7**, 1139 (2020).
- [13] W. C. Jiang, X. Lu, J. Zhang, O. Painter, and Q. Lin, Silicon-chip source of bright photon pairs, *Opt. Express* **23**, 20884 (2015).
- [14] N. M. Lüpken, D. Becker, T. Würthwein, K.-J. Boller, and C. Fallnich, Toward integrated synchronously pumped optical parametric oscillators in silicon nitride, *Opt. Express* **29**, 39895 (2021).
- [15] M. He and K. Jamshidi, in *Nonlinear Optics and its Applications 2022*, Vol. 12143 (SPIE, Strasbourg, France, 2022), p. 23.
- [16] X. Ji, F. A. Barbosa, S. P. Roberts, A. Dutt, J. Cardenas, Y. Okawachi, A. Bryant, A. L. Gaeta, and M. Lipson, Ultra-low-loss on-chip resonators with sub-milliwatt parametric oscillation threshold, *Optica* **4**, 619 (2017).
- [17] D. J. Blumenthal, R. Heideman, D. Geuzebroek, A. Leinse, and C. Roeloffzen, Silicon nitride in silicon photonics, *Proc. IEEE* **106**, 2209 (2018).
- [18] M. W. Puckett, K. Liu, N. Chauhan, Q. Zhao, N. Jin, H. Cheng, J. Wu, R. O. Behunin, P. T. Rakich, and K. D. Nelson, *et al.*, 422 million intrinsic quality factor planar integrated all-waveguide resonator with sub-MHz linewidth, *Nat. Commun.* **12**, 934 (2021).
- [19] E. F. Perez, G. Moille, X. Lu, J. Stone, F. Zhou, and K. Srinivasan, High-performance Kerr microresonator optical parametric oscillator on a silicon chip, *Nat. Commun.* **14**, 242 (2023).
- [20] W. Wang, S. T. Chu, B. E. Little, A. Pasquazi, Y. Wang, L. Wang, W. Zhang, L. Wang, X. Hu, and G. Wang, *et al.*, Dual-pump Kerr micro-cavity optical frequency comb with varying FSR spacing, *Sci. Rep.* **6**, 1 (2016).
- [21] Y. Okawachi, B. Y. Kim, Y. Zhao, X. Ji, M. Lipson, and A. L. Gaeta, in *CLEO: Science and Innovations* (Optica Publishing Group, San Jose, California, United States, 2021), p. SW3R-2.
- [22] D. T. Spencer, T. Drake, T. C. Briles, J. Stone, L. C. Sinclair, C. Fredrick, Q. Li, D. Westly, B. R. Ilic, and A. Bluestone, *et al.*, An optical-frequency synthesizer using integrated photonics, *Nature* **557**, 81 (2018).
- [23] N. M. Lüpken, T. Würthwein, J. P. Epping, K.-J. Boller, and C. Fallnich, Spontaneous four-wave mixing in silicon nitride waveguides for broadband coherent anti-Stokes Raman scattering spectroscopy, *Opt. Lett.* **45**, 3873 (2020).
- [24] Y. Zhao, Y. Okawachi, J. K. Jang, X. Ji, M. Lipson, and A. L. Gaeta, Near-degenerate quadrature-squeezed vacuum generation on a silicon-nitride chip, *Phys. Rev. Lett.* **124**, 193601 (2020).
- [25] J. R. Stone, G. Moille, X. Lu, and K. Srinivasan, Conversion efficiency in Kerr-microresonator optical parametric

- oscillators: From three modes to many modes, *Phys. Rev. Appl.* **17**, 024038 (2022).
- [26] M. Jazayerifar, M. Namdari, R. Hamerly, D. Gray, C. Rogers, and K. Jamshidi, in *Integrated Optics: Devices, Materials, and Technologies XXI*, Vol. 10106 (SPIE, San Jose, California, United States, 2017), p. 45.
- [27] M. Jankowski, A. Marandi, C. Phillips, R. Hamerly, K. A. Ingold, R. L. Byer, and M. Fejer, Temporal simultons in optical parametric oscillators, *Phys. Rev. Lett.* **120**, 053904 (2018).
- [28] C. Fabre, The optical Ising machine, *Nat. Photonics* **8**, 883 (2014).
- [29] Y. Okawachi, M. Yu, K. Luke, D. O. Carvalho, S. Ramelow, A. Farsi, M. Lipson, and A. L. Gaeta, Dual-pumped degenerate Kerr oscillator in a silicon nitride microresonator, *Opt. Lett.* **40**, 5267 (2015).
- [30] D. Gray, R. Hamerly, M. Namdari, M.-T. Cătuneanu, K. Jamshidi, N. Bogdanowicz, and H. Mabuchi, Thermo-optic multistability and relaxation in silicon microring resonators with lateral diodes, *Phys. Rev. Appl.* **14**, 024073 (2020).
- [31] A. Roy, S. Jahani, C. Langrock, M. Fejer, and A. Marandi, Spectral phase transitions in optical parametric oscillators, *Nat. Commun.* **12**, 1 (2021).
- [32] R. Hamerly, D. Gray, C. Rogers, L. Mirzoyan, M. Namdari, and K. Jamshidi, in *Physics and Simulation of Optoelectronic Devices XXV*, Vol. 10098 (SPIE, San Francisco, California, United States, 2017), p. 16.
- [33] J. Liu, G. Huang, R. N. Wang, J. He, A. S. Raja, T. Liu, N. J. Engelsen, and T. J. Kippenberg, High-yield, wafer-scale fabrication of ultralow-loss, dispersion-engineered silicon nitride photonic circuits, *Nat. Commun.* **12**, 1 (2021).
- [34] A. E. Fomin, M. L. Gorodetsky, I. S. Grudinin, and V. S. Ilchenko, Nonstationary nonlinear effects in optical microspheres, *JOSA B* **22**, 459 (2005).
- [35] T. Gu, M. Yu, D.-L. Kwong, and C. W. Wong, Molecular-absorption-induced thermal bistability in PECVD silicon nitride microring resonators, *Opt. Express* **22**, 18412 (2014).
- [36] C. Zhang, G.-G. Kang, J. Wang, S. Wan, C.-H. Dong, Y.-J. Pan, and J.-F. Qu, Photonic thermometer by silicon nitride microring resonator with milli-kelvin self-heating effect, *Measurement* **188**, 110494 (2022).
- [37] M. Borghi, D. Bazzanella, M. Mancinelli, and L. Pavesi, On the modeling of thermal and free carrier nonlinearities in silicon-on-insulator microring resonators, *Opt. Express* **29**, 4363 (2021).
- [38] F. A. Sabattoli, H. El Dirani, L. Youssef, F. Garrisi, D. Grassani, L. Zatti, C. Petit-Etienne, E. Pargon, J. Sipe, and M. Liscidini, *et al.*, Suppression of parasitic nonlinear processes in spontaneous four-wave mixing with linearly uncoupled resonators, *Phys. Rev. Lett.* **127**, 033901 (2021).
- [39] Z. Yang, M. Jahanbozorgi, D. Jeong, S. Sun, O. Pfister, H. Lee, and X. Yi, A squeezed quantum microcomb on a chip, *Nat. Commun.* **12**, 1 (2021).
- [40] W. Xing and T. Ralph, Pump depletion in parametric amplification, Preprint [ArXiv:2201.01372](https://arxiv.org/abs/2201.01372) (2022).
- [41] R. Hamerly and H. Mabuchi, Optical devices based on limit cycles and amplification in semiconductor optical cavities, *Phys. Rev. Appl.* **4**, 024016 (2015).
- [42] M. Nie and S.-W. Huang, Quadratic solitons in singly resonant degenerate optical parametric oscillators, *Phys. Rev. Appl.* **13**, 044046 (2020).
- [43] L. Hill, G.-L. Oppo, M. T. Woodley, and P. Del'Haye, Effects of self-and cross-phase modulation on the spontaneous symmetry breaking of light in ring resonators, *Phys. Rev. A* **101**, 013823 (2020).
- [44] R. Deb and P. S. Maji, Dual pump broadband fiber-optic parametric amplifier based on near-zero dispersion photonic crystal fiber with single zero dispersion wavelength, *Opt. Eng.* **60**, 036108 (2021).
- [45] R. Hamerly, D. Gray, C. Rogers, and K. Jamshidi, Conditions for parametric and free-carrier oscillation in silicon ring cavities, *J. Lightwave Technol.* **36**, 4671 (2018).
- [46] P. A. Andrekson and M. Karlsson, Fiber-based phase-sensitive optical amplifiers and their applications, *Adv. Opt. Photonics* **12**, 367 (2020).
- [47] D. Heydari, M. Cătuneanu, E. Ng, D. J. Gray, R. Hamerly, J. Mishra, M. Jankowski, M. Fejer, K. Jamshidi, and H. Mabuchi, Degenerate optical parametric amplification in CMOS silicon, *Optica* **10**, 430 (2023).
- [48] M. Karpov, M. H. Pfeiffer, H. Guo, W. Weng, J. Liu, and T. J. Kippenberg, Dynamics of soliton crystals in optical microresonators, *Nat. Phys.* **15**, 1071 (2019).
- [49] H. Guo, M. Karpov, E. Lucas, A. Kordts, M. H. Pfeiffer, V. Brasch, G. Lihachev, V. E. Lobanov, M. L. Gorodetsky, and T. J. Kippenberg, Universal dynamics and deterministic switching of dissipative Kerr solitons in optical microresonators, *Nat. Phys.* **13**, 94 (2017).
- [50] T. Herr, V. Brasch, J. D. Jost, C. Y. Wang, N. M. Kondratiev, M. L. Gorodetsky, and T. J. Kippenberg, Temporal solitons in optical microresonators, *Nat. Photonics* **8**, 145 (2014).